Genomic Structure of *Hstx2* Modifier of *Prdm9*-Dependent Hybrid Male Sterility in Mice

Diana Lustyk,*,† Slavomír Kinský,‡ Kristian Karsten Ullrich,§ Michelle Yancoskie, Lenka Kašíková,*,1,2 Vaclav Gergelits,* Radislav Sedlacek,‡ Yingguang Frank Chan,** Linda Odenthal-Hesse,§ Jiri Forejt,*,3 and Petr Jansa*,3**

*Laboratory of Mouse Molecular Genetics and ‡The Czech Centre for Phenogenomics, Division BIOCEV, Institute of Molecular Genetics, Czech Academy of Sciences, Vestec CZ-25250, Czech Republic, †Faculty of Science, Charles University, Prague CZ-12000, Czech Republic, §Department Evolutionary Genetics, Research Group Meiotic Recombination and Genome Instability, Max Planck Institute for Evolutionary Biology, Plön D-24306, Germany, and **Molecular Basis and Evolution of Complex Traits Group, Friedrich Miescher Laboratory of the Max Planck Society, Tübingen 72076, Germany

ORCID IDs: 0000-0003-0879-4012 (D.L.); 0000-0003-4308-9626 (K.K.U.); 0000-0002-5178-8833 (V.G.); 0000-0002-3352-392X (R.S.); 0000-0001-6292-9681 (Y.F.C.); 0000-0002-5519-2375 (L.O.-H.); 0000-0002-2793-3623 (J.F.); 0000-0002-1406-1707 (P.J.)

ABSTRACT F_1 hybrids between mouse inbred strains PWD and C57BL/6 represent the most thoroughly genetically defined model of hybrid sterility in vertebrates. Hybrid male sterility can be fully reconstituted from three components of this model, the *Prdm9* gene, intersubspecific homeology of *Mus musculus musculus* and *Mus musculus domesticus* autosomes, and the X-linked *Hstx2* locus. *Hstx2* modulates the extent of *Prdm9*-dependent meiotic arrest and harbors two additional factors responsible for intersubspecific introgression-induced oligospermia (*Hstx1*) and meiotic recombination rate (*Meir1*). To facilitate positional cloning and to overcome the recombination suppression within the 4.3 Mb encompassing the *Hstx2* locus, we designed *Hstx2*-CRISPR and SPO11/Cas9 transgenes aimed to induce DNA double-strand breaks specifically within the *Hstx2* locus. The resulting recombinant reduced the *Hstx2* locus to 2.70 Mb (chromosome X: 66.51–69.21 Mb). The newly defined *Hstx2* locus still operates as the major X-linked factor of the F_1 hybrid sterility, and controls meiotic chromosome synapsis and meiotic recombination rate. Despite extensive further crosses, the 2.70 Mb *Hstx2* interval behaved as a recombination cold spot with reduced PRDM9-mediated H3K4me3 hotspots and absence of DMC1-defined DNA double-strand-break hotspots. To search for structural anomalies as a possible cause of recombination suppression, we used optical mapping and observed high incidence of subspecies-specific structural variants along the X chromosome, with a striking copy number polymorphism of the microRNA *Mir465* cluster. This observation together with the absence of a strong sterility phenotype in Fmr1 neighbor (*Fmr1nb*) null mutants support the role of microRNA as a likely candidate for *Hstx2*.

KEYWORDS Speciation; Hybrid sterility X2; *Prdm9*; Bionano optical mapping; SPO11Cas9 transgene; *Fmr1nb*

REPRODUCTIVE isolation is a basic prerequisite of speciation implemented by a range of prezygotic and postzygotic mechanisms under complex genetic control (Dobzhansky 1951; Dion-Côté and Barbash 2017). Hybrid sterility, one of the reproductive isolation mechanisms, appears in the early stages of speciation and shares common features in many animal and plant species hybrids. They include preferential involvement of the heterogametic sex (XY or ZW), known as Haldane's rule (Haldane 1922), or the large X effect (Coyne's rule), referring to disproportionate engagement of X chromosome compared to autosomes (Dobzhansky 1951; Forejt 1996; Coyne and Orr 2004; Good *et al.* 2008; Presgraves 2018). The first hypothesis on genetic control of hybrid sterility, known as Dobzhansky–Muller epistatic incompatibility, refers to a dysfunction caused by the independent divergence of mutually interacting genes (Dobzhansky 1951). More recently, an interaction between meiotic drive and its suppressors has

doi: https://doi.org/10.1534/genetics.119.302554
Manuscript received August 16, 2019; accepted for publication September 23, 2019; published Early Online September 26, 2019.
Supplemental material available at FigShare: https://doi.org/10.25386/genetics.9874460.
[1]Present address: Department of Immunology, Charles University, Second Faculty of Medicine and University Hospital Motol, Prague CZ-15000, Czech Republic.
[2]Present address: SOTIO, Prague CZ-17000, Czech Republic.
[3]Corresponding authors: Laboratory of Mouse Molecular Genetics, Division BIOCEV, Institute of Molecular Genetics, Czech Academy of Sciences, Prumyslova 595, Vestec CZ-25250, Czech Republic. E-mail: pjansa@img.cas.cz; and jforejt@img.cas.cz

been implicated in some instances of reproductive isolation (Orr 2005; Zhang *et al.* 2015; Patten 2018). However, despite extensive genetic studies in organisms of various species such as yeast, fruit fly, or house mouse, the underlying genetic architecture and molecular mechanisms of hybrid sterility remain elusive [reviewed in Maheshwari and Barbash (2011); Phifer-Rixey and Nachman (2015); Dion-Côté and Barbash (2017); Mack and Nachman (2017); Payseur *et al.* (2018)].

The first hybrid sterility genetic factor to be identified in vertebrate, the hybrid sterility 1 (*Hst1*), was described in hybrids between laboratory and wild mice (Forejt and Ivanyi 1974; Gregorová *et al.* 1996; Trachtulec *et al.* 1997) and identified as the *Prdm9* gene encoding PR/SET domain-containing nine protein (Mihola *et al.* 2009). The PRDM9 binds genomic DNA by a zinc finger domain at allele-specific sites and trimethylates lysine 4 and lysine 36 of histone 3. In mice, humans, and other mammalian species, *Prdm9* mediates meiotic recombination by determining the genomic localization of the recombination hotspots (Baudat *et al.* 2010; Myers *et al.* 2010; Parvanov *et al.* 2010). In a mouse model of intersubspecific hybrids where *Mus musculus domesticus* subspecies is represented by inbred strain C57BL/6J (hereafter B6) and *Mus musculus musculus* by PWD/Ph (hereafter PWD) (Gregorova and Forejt 2000) *Prdm9* causes early meiotic arrest and complete male sterility by interaction with the X-linked *Hstx2* locus. Hybrids between laboratory strains PWD and B6 serve as a robust, reproducible and genetically well-defined model of hybrid sterility [reviewed in Forejt (1996); Forejt *et al.* (2012)]. Specific allelic combinations of the *Prdm9* gene ($Prdm9^{PWD/B6}$) and *Hstx2* locus ($Hstx2^{PWD}$) were shown necessary but not sufficient to fully explain the meiotic arrest in hybrids. Initially, three or more additional hybrid sterility genes of small effect complementing the *Prdm9* and *Hstx2* major hybrid sterility genes had been considered (Dzur-Gejdosova *et al.* 2012). Later, we identified chromosome-autonomous meiotic asynapsis of homeologous chromosomes [homologous chromosomes from related (sub)species] as the third requirement for meiotic arrest (Bhattacharyya *et al.* 2013, 2014). The chromosomal, nongenic effects of homeologous chromosomes in (PWD × B6) F_1 hybrids, manifested as a failure of meiotic chromosome synapsis, is most likely a consequence of evolutionary erosion of PRDM9 binding sites in each subspecies, resulting in asymmetry of DNA double-strand-break (DSB) hotspots (Davies *et al.* 2016). The explanation of hybrid sterility by expected shortage of symmetric DNA DSBs was supported by improvement of chromosome pairing and fertility after experimentally increasing the number of symmetric DNA DSBs by random stretches of a homozygous PWD sequence (Gregorova *et al.* 2018). Moreover, partial improvement of meiotic chromosome synapsis in hybrid males was achieved by addition of exogenous DSBs generated by a single cisplatin injection (Wang *et al.* 2018).

The PWD allele of the *Hstx2* locus ($Hstx2^{PWD}$) is indispensable for full sterility of (PWD × B6) F_1 hybrids, while the $Hstx2^{B6}$ allele attenuates the phenotype to partial spermatogenesis arrest in reciprocal (B6 × PWD) F_1 males (Dzur-Gejdosova *et al.* 2012; Flachs *et al.* 2012; Forejt *et al.* 2012). Admittedly, the mechanism of action of the *Hstx2* locus in meiotic arrest of F_1 hybrids remains elusive. Previously, the *Hstx2* locus was mapped to a 4.7 Mb region on X chromosome [chromosome X (Chr X): 64.9–69.6 Mb] (Bhattacharyya *et al.* 2014). The interval that encompasses 10 protein-coding genes and a cluster of microRNA (miRNA) genes is still too large to identify the true *Hstx2* candidate. The *Hstx2* locus (Chr X: 64.9–69.6 Mb) harbors two additional meiosis-related genetic factors, the hybrid sterility X1 (*Hstx1*) locus, manifested by sperm head malformations after $Hstx2^{PWD}$ sequence introgression into the B6 genome (Storchová *et al.* 2004), and meiotic recombination 1 (*Meir1*), which controls meiotic recombination rate (Balcova *et al.* 2016). Since these factors have not yet been genetically separated, their phenotypes may represent a pleiotropic effect of the same gene.

In an attempt to reduce the size of *Hstx2*, we constructed an SPO11-driven CRISPR-Cas9 system to target meiotic recombination to a particular genomic locus within the *Hstx2* recombination cold spot. Although the method did not work as predicted, we recovered a single recombinant, thus reducing the *Hstx2* locus to 2.70 Mb. We show that the shortened version of *Hstx2* still carries the genetic factors or genes responsible for hybrid sterility, meiotic chromosome asynapsis, and genome-wide control of meiotic recombination rate. Using Bionano Optical mapping technology, we show high incidence of subspecies-specific insertion/deletion variants inside and outside the *Hstx2* locus. Furthermore, we interrogate the *Fmr1nb* gene as a possible *Hstx2* candidate gene.

Materials and Methods

Animals and ethics statement

The mice were maintained in the Pathogen-Free Facility of the Institute of Molecular Genetics (Czech Academy of Sciences in Prague). The project was approved by the Animal Care and Use Committee of the Institute of Molecular Genetics AS CR and by the Czech Central Committee for Animal Welfare, and ethically reviewed and performed in accordance with European Directive 86/609/EEC. Subconsomic mouse strains C57BL/6J-ChrX.1^{PWD}/Ph (abbreviated B6.DX.1) and C57BL/6J-ChrX.1s^{PWD}/Ph (B6.DX.1s) were described earlier (Storchová *et al.* 2004). The C57BL/6J-ChrX.64-69$^{PWD/Ph}$/ForeJ (B6.DX.64-69) congenic strain was established by backcrossing B6.DX.1s to the B6 strain (Figure 1). The congenic strain C57BL/6J-ChrX.66-69^{PWD}/Ph (B6.DX.66-69) was prepared by the new CRISPR/ Cas9 *Hstx2*-targeting method. The PWD/B6 composition of the Chr X is depicted schematically in Figure 1 for each consomic strains.

Genotyping, fertility parameters, and histology

Genomic DNA was prepared from tails by NaOH method (Truett *et al.* 2000). The X chromosome recombinants in

the backcross 1 (BC1) populations were genotyped by PWD/B6 allele-specific microsatellite markers (Supplemental Material, Table S1). Recombination breakpoints were determined by Sanger-DNA sequencing of the PCR amplicons carrying informative PWD/B6 SNP polymorphism(s). Genotyping of the new B6.DX.66-69 strain by microsatellite markers, Sanger DNA sequencing, and next-generation sequencing showed the maximum and minimum extent of the PWD sequence on Chr X. The *Fmr1nb* deletion was confirmed using primers: forward 5′CAGGAGGTTCTGGACTGCTC 3′ and reverse 5′TGAAGTCCAGAAGCCAAACC 3′. All experiments were performed with at least three animals per group. Cytological and histological experiments were performed on males between 8 and 10 weeks of age, with the exception of the males after fertility test.

Quantitative Reverse Transcription-PCR (RT-qPCR) analysis

Total RNA was extracted from testes by TRI reagent #T9424 (Sigma, St. Louis, MO) according to manufacturer's instructions. The RNA was reverse transcribed using MuMLV-RT (28025-013; Invitrogen, Carlsbad, CA). Quantitative real-time PCR was performed with the Light Cycler DNA Fast Start Master SYBR Green I kit (Roche) in a Light Cycler 480 Instrument II at Tm = 60°. The sequences of primers for *Fmr1nb* were: Fmr1nb-F – 5′-TCCTGGGATTTCTGCCTATG-3′, Fmr1nb-R – 5′-CCTTCAACATCCTGTTCATCC-3′; and the primers for *Actin-b* were: Actb-F – 5′-CTAAGGCCAACCGT GAAAAG-3′, Actb-R – 5′-ACCAGAGGCATACAGGGACA-3′. The *Fmr1nb* expression values were normalized to *Actin-b* expression.

Western blotting

Whole testes were snap-frozen in liquid nitrogen before extraction buffer with protease inhibitors (1836153; Roche) and bensonase (1.01654.0001; Merck) was used to homogenize the tissue (see supplementary Reagent Table). After a 30 min incubation, 2% SDS was added and the mixture was heated at 95° for 20 min. Total protein concentration was measured using the Pierce BCA Protein Assay Kit (#23225; Thermo Scientific). The protein samples were then size-separated by electrophoresis on a gradient Bolt 4–12% Bis-Tris plus gel (NW04120BOX; Invitrogen), transferred onto a polyvinylidene difluoride membrane, and blocked with TBST with 5% BSA overnight. Primary antibodies against FMR1NB (sc-246953, goat polyclonal; Santa Cruz Biotechnology) and alpha-tubulin (66031-1-Ig, mouse monoclonal; Proteintech) were used at the 1:1000 and 1:2000 dilutions, respectively. Secondary antibodies (a donkey anti-goat IgG-HRP antibody, sc-2020; Santa Cruz Biotechnology, and a horse anti-mouse IgG-HRP antibody, 7076; Cell Signaling Technology) conjugated to HRP were used at 1:10000 dilution. Western Blotting Substrate (#32106; Pierce ECL Plus) was used for detection of HRP enzyme activity. Images were captured using the Bio-Rad ChemiDoc MP Imaging System and processed with ImageLab software (Bio-Rad, Hercules, CA).

Immunofluorescence microscopy

Meiotic chromosome spreads were performed as previously described (Anderson *et al.* 1999) with minor modifications. Briefly, the testes were dissected and transferred to 1 ml of RPMI (Sigma). Sucrose (0.1 M) was used as a hypotonic solution and cells were dropped onto a slide with 1% paraformaldehyde containing protease inhibitors (1836153; Roche). After 3 hr at 4° slides were washed and blocked with 0.5 × blocking buffer (1.5% BSA, 5% goat serum, 0.05% Triton X-100) containing protease inhibitors (1836153; Roche) for 1 hr at 4°. Primary antibodies (listed in supplementary Reagent Table) were added and the slides were incubated overnight in a humid chamber at 4°. The slides were then incubated with secondary antibodies conjugated to fluorophores (supplementary Reagent table) for 1 hr at 4°. The slides were mounted with Vectashield mounting medium containing DAPI (H1200). The immunofluorescence images were observed by Nikon Eclipse ×400 epifluorescence microscope with single band-pass filters for excitation and emission of infrared, red, blue, and green fluorescence (Chroma Technologies) and ×60 Plan Fluor objective (MRH00601; Nikon, Garden City, NY). The images were captured using a DS-QiMc monochrome CCD camera (Nikon) and NIS Elements processing program (NIS-Elements Microscope Imaging Software). The images were adjusted using Adobe Photoshop (Adobe Systems).

Construction of Fmr1nb-specific TALEN and generation of transgenic mice

TALEN nucleases were designed using TAL Effector Nucleotide Targeter 2.0 (https://tale-nt.cac.cornell.edu/), assembled using the Golden Gate Cloning system (https://international.neb.com/applications/cloning-and-synthetic-biology/dna-assembly-and-cloning/golden-gate-assembly), and cloned into the ELD-KKR backbone plasmid. TALEN containing repeats NN-NN-HD-NG-NN-NN-NG-NG-NI-NN-NI-NN-NI-HD-HD-NG-HD-HD (for 5′ site) and NG-HD-NG-HD-NG-NN-NI-HD-NG-NG-NN-NN-HD-HD-NG-NG (for 3′ site) recognized a locus close to the ATG start codon of *Fmr1nb*. Each TALEN plasmid was linearized with *Not*I and transcribed using the mMESSAGE mMACHINE T7 Kit (Ambion). Polyadenylation of resulting messenger RNAs (mRNAs) was performed using the Poly(A) Tailing Kit (Ambion); the mRNA was purified with RNeasy Mini columns (Qiagen, Valencia, CA). TALEN mRNAs were diluted in nuclease free water and kept at −80°. Transgenic mice were generated in the transgenic facility of the Institute of Molecular Genetics by injecting purified mRNA of *Fmr1nb*-specific TALEN into male pronuclei of one-cell embryos of C57BL/6N or B6.DX.1s origin. Mice positive for mutations were identified by PCR reaction with Fmr1nb2outF and Fmr1RightBsrI primers followed by *Nsp*I digestion. Specific genome mutations were identified by PCR fragment sequencing. Twenty-three mouse founders (F_0), each carrying a mutated allele of the *Fmr1nb* gene, were generated. After outcrossing the F_0 mice

to C57BL/6N or to B6.DX.1s we obtained five B6.*Fmr1nb*$^{-}$ mouse strains and three B6.DX.1s.*Fmr1nb*$^{-}$ strains with stable deletion mutations. Here we used two lines, the B6.*Fmr1nb*^{em1ForeJ} line carrying 236 bp long deletion over the ATG start codon of the *Fmr1nb*^{B6} allele, and the B6.DX.1s.*Fmr1nb*^{em1ForeJ} line carrying 19 bp long deletion over the ATG start codon of the of *Fmr1nb*^{PWD} allele.

Preparation of CRISPR-Hstx2 and SPO11-Cas9 constructs, and generation of transgenic mice

To place the Cas9 nuclease under the control of the SPO11 promoter, the SPO11 coding region was replaced by a mouse codon-optimized Cas9 open reading frame in an SPO11-carrying bacterial artificial chromosome (BAC) clone (RP23-20N4, distributed by BACPAC Resources, Oakland, CA) by a marker-less GalK double-selection system via liquid culture recombineering as described (Sharan *et al.* 2009). Homology arms for the SPO11 BAC were introduced by PCR with Phusion polymerase (New England Biolabs, Frankfurt am Main, Germany). The 1.3 kbp PCR product was purified with a Gel Extraction Kit (QIAGEN) and confirmed by Sanger sequencing. The Cas9 cassette was produced by excision from plasmid MLM3613 (#42251; Addgene, Watertown, MA) by enzymes *Sac*II and *Mss*I (Thermo Fisher Scientific, Schwerte, Germany) and purified by gel extraction. The homology arms were added by PCR amplification and Phusion polymerase. The CRISPR plasmid pX260 was obtained (#42229, Addgene plasmid, a gift from Feng Zhang; Cong *et al.* 2013) and the CRISPR protospacers corresponding to the *Hstx2* loci were cloned according to instructions from the Zhang Laboratory (https://media.addgene.org/cms/filer_public/e6/5a/e65a9ef8-c8ac-4f88-98da-3b7d7960394c/zhang-lab-general-cloning-protocol.pdf). Briefly, long oligonucleotides were ordered as Ultramers (oligos 20–21; Integrated DNA Technologies, Coralville, IA) for the following three target regions flanking the *Hstx2* locus: a sequence 2.2 Mb upstream of the *Ctag2* gene (Chr X: 65,069,229–65,069,258); an intergenic sequence between the *Mir465* cluster and *Gm1140* predicted protein coding gene (Chr X: 67,052,342–67,052,371); and a sequence 4 kbp upstream of the *Aff2* gene (Chr X: 69,356,143–69,356,172). After phosphorylation (T4 Polynucleotide Kinase, New England Biolabs) and annealing by temperature ramping from 95° to 30 sec by −0.1°/min increments, the duplexes were ligated into the *Bbs*I site of the cut pX260 plasmid (New England Biolabs) and transformed into DH5-Alpha *Escherichia coli* cells. The protospacer-containing plasmids were further modified by excising the Cas9 open reading frame with *Pst*I (New England Biolabs). Each final plasmid contains the U6 promoter, protospacer, the ^{1}H promoter, and the *trans*-activating CRISPR RNA. These were sequence-verified before transgenic injection. The CRISPR constructs and SPO11-Cas9-BAC construct were generated in Tubingen by the laboratory of Y.F.C. The BAC transgene was injected to the pronuclei of 1-day-old mouse embryos and the founders were generated in the laboratory of R.S. in Vestec.

Bionano optical mapping

We generated optical maps for two markers (BspQ1 and DLE-1) across the whole genome of five different mice, from two mouse subspecies: C57BL/6J (B6) and C57Bl6Crl (B6N) of *M. m. domesticus* and PWD/Ph (PWD) and PWK/Ph (PWK) of *M. m. musculus* origin. Two females were from the congenic C57BL/6J-ChrX.64-69PWD/Ph strain (B6.DX64-69), carrying a small portion of Chr X including the hybrid sterility *Hstx2* locus from PWD/Ph on C57BL/6 background. First, megabase-scale high-molecular-weight (HMW) DNA was extracted according to the Saphyr Bionano Prep Animal Tissue DNA Isolation Soft Tissue Protocol (Document Number: 30077, Revision B). Briefly, cell nuclei were isolated from splenic tissue and embedded in agarose plugs. DNA in plugs was purified with Proteinase K and RNAse, then HMW genomic DNA was extracted from the agarose plugs using agarase, and purified by drop dialysis. HMW DNA was resuspended overnight before quantification with the Qubit BR dsDNA assay, then kept at 4° until labeling. Each sample was labeled at the recognition sites NtBspQ1 (GCTCTTC) and DLE-1 (CTTAAG), respectively, using two different methylation insensitive assays. The Bionano nicking, labelling, repairing, and staining protocol was used to label NtBspQ1 (Document Number: 30206, Revision C), and was performed on 900 ng of purified HMW DNA for each mouse. The Bionano direct labelling and staining protocol (Document Number: 30024, Revision I) was performed on 750 ng of DNA to label all DLE-1 recognition sites. After an initial clean-up step, the labeled HMW DNA was prestained, homogenized, and quantified with the Qubit HS dsDNA assay, before using an appropriate amount of backbone stain YOYO-1. The molecules were then imaged using the Bionano Saphyr System (Bionano Genomics, San Diego, CA). We obtained high-quality optical reads for both labeling techniques. For example, for the nicking, labelling, repairing, and staining labeling produced an average of 437 Gbps of reads, which were longer than 150 kbps and have a minimum of nine label. It achieved an average N50 length of 0.3137 Mbp with an average label density of 14.82 labels per 100 kbp. Similarly, the direct labelling and staining labeling achieved an average output of 389 Gbps ($\geq$150 kbp and minSites $\geq$9), an average N50 length of 0.2663 Mbp and an average label density of 13.72/100 kbp. (Individual outputs were collected for each animal and labeling technique in Table S2). The presence of *in silico* recognition sites for each enzyme recognition site in the genome was used to compute separate *in silico* optical maps for each labeling enzyme, for the mm10 genome (Table S3).

Detection and quantification of apoptotic cells: terminal deoxynucleotidyl transferase-mediated dUTP nick-end labeling assay

The males were killed and the testes dissected from, and fixed in 4% paraformaldehyde overnight at 4°. Testes were dehydrated and embedded in paraffin. Paraffin sections at 3 μm thick were deparaffinized. To perform antigen retrieval for

immunohistochemistry, the slides were incubated in Citrate Antigen Retrieval solution for 15 min at pH 6.0. The slides were processed as for immunofluorescence. The apoptotic cells in the tissue sections were determined by terminal deoxynucleotidyl transferase-mediated dUTP nick-end labeling (TUNEL), using *in situ* DeadEnd Fluorometric detection kit (G3250-PROMEGA, Madison, WI) according to technical protocol (#TB235). TUNEL-treated testicular sections were mounted in Vectashield with DAPI to watch the nuclei. Images were captured from a Nikon E-400 Eclipse fluorescence microscope and captured with a Ds-Qi_Mc1 CCD camera (Nikon). The images were processed and TUNEL-positive cells counted by the NIS Elements picture analyzer, and processed using Photoshop (Adobe).

Fertility test

Each male was mated with one 8-week-old C57BL/6J virgin female for 3 months, during which the numbers of neonatal pups sired by B6.DX.1s.Fmr1nb^{-} and B6.DX.1s males were recorded.

Data availability and statistics

Strains and plasmids are available upon request. The authors affirm that all data necessary for confirming the conclusions of the article are present within the article, figures, tables, and in the supplemental material. The optical mapping data sets are available from L.O.-H. or K.K.U. upon reasonable request. Statistical analyses were performed by unpaired two-tailed *t*-test, if not indicated otherwise. Statistical significance was set at *P* values of * 0.05,** 0.01, and *** 0.005. Data were processed and plotted by GraphPad Prism version 6.00 (GraphPad Software, San Diego, CA; www.graphpad.com). Other types of statistical analyses are described within the text and in the corresponding figure legends. Supplemental material available at FigShare: https://doi.org/10.25386/genetics.9874460.

Results

Hstx2 locus is a recombination cold spot

The *Hstx2* locus was initially defined as a 4.7 Mb PWD interval present in B6.PWD-Chr X.1s (B6.DX.1s), but absent in the partially overlapping B6.PWD-Chr X.1 (abbreviated B6.DX.1) congenic strain. (Storchová *et al.* 2004; Bhattacharyya *et al.* 2014) (Figure 1A).

Here, we specified the PWD/B6 distal border of B6.PWD-Chr X.1s by next-generation sequencing to Chr X: 69.21 Mb narrowing the *Hstx2* locus to 4.3 Mb of the PWD sequence (Figure 1A). Admittedly, such subtraction mapping could not exclude the possibility that some additional genetic information in the proximal 64.9 Mb of the PWD sequence may contribute to the genetic factors situated within *Hstx2* locus. To reduce the size of *Hstx2* locus and to check the possible role of the proximal region of the X^{PWD} sequence, 52 new recombinant X chromosomes were generated in three BC1

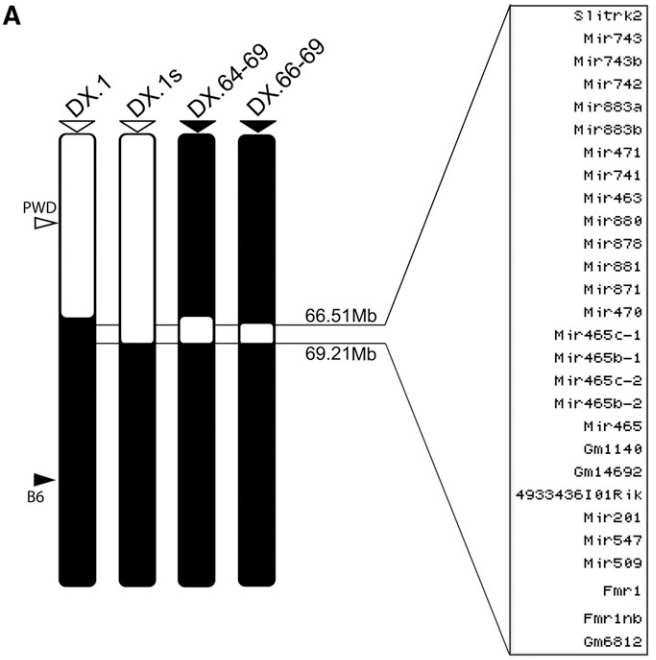

B

Strain	n	Testes weight (mg)	Sperm Count ($x10^6$)	Sperm head malformation rate (%)
DX.1	9	187.4 ± 12.2	50.4 ± 12.5	24.8 ± 2.2
DX.1s	14	171.9 ± 8.8	53.5 ± 10.0	69.0 ± 7.2
DX.64-69	9	169.4 ± 26.3	50.5 ± 14.5	40.8 ± 2.8
DX.66-69	5	154.8 ± 5.0	31.3 ± 8.4	40.3 ± 4.9

C

Cross	n	Testes weight (mg)	Sperm Count ($x10^6$)
(B6 x PWD)F1	42	102.3 ± 9.4	6.2 ± 3.9
(DX.1 x PWD)F1	3	106.0 ± 8.0	7.4 ± 4.6
(PWD x B6)F1	5	65.2 ± 1.9	0.01 ± 0.02
(DX.1s x PWD)F1	20	62.3 ± 2.9	0.01 ± 0.02
(DX.64-69 x PWD)F1	25	54.7 ± 6.4	0.004 ± 0.01
(DX.66-69 x PWD)F1	20	55.5 ± 5.1	0.01 ± 0.04

Figure 1 Mapping of hybrid male sterility *Hstx1* and *Hstx2* loci in subconsomic and congenic strains. (A) Schematic view of the chromosome X architecture in subconsomic and congenic strains B6.DX.1, B6.DX.1s, B6.DX.64-69, and B6.DX.66-69. The PWD and B6 origin of chromosomal intervals is depicted in white and black. The list of protein coding genes, noncoding RNAs, and miRNAs spanning the interval of the newly defined *Hstx2* locus (66.51–69.21 Mb) is shown. (B) *Hstx1* locus mapping. Fertility parameters of subconsomic and congenic males; the testes weight (weight of wet testes pair in milligrams), the sperm count (number of sperms in millions per pair of epididymes), and frequency of malformed sperm heads (in percent). (C) *Hstx2* locus mapping. Fertility parameters of the (B6 × PWD) F_1 and the reciprocal (PWD × B6) F_1 hybrid males, and F_1 male progeny of crosses of B6.DX.1, B6.DX.1s, B6.DX.64-69, and B6.DX.66-69 congenic females with PWD males are presented as mean ± SD; *n*, number of analyzed males.

populations (Table 1). Genotyping of 168 (B6.DX.1s × B6) × B6 BC1 mice yielded 51 recombinants with crossovers spanning the proximal region of Chr X. A new C57BL/6J-ChrX.64-69$^{PWD/Ph}$ congenic strain (abbreviated B6.DX.64-69)

Table 1 Localization of PWD/B6 recombination events on the X chromosome

Backcross (BC1)	Number of BC1 (*n*)	Number of recombination events (*N*) in the specific X chromosome intervals / recombination rate[a,b] (cM/Mb)				
		X:7.36–65.10 Mb	X:7.36–36.20 mb	X:36.20–59.66 Mb	X:59.66–65.10 Mb	X:65.10–69.08 Mb
DX.1s × B6) × B6	168	51 / 0.526[a]	17 / 0.351[a]	30 / 0.761[a]	4 / 0.438[a]	0
(DX.51-69 × B6) × B6	111	N.D.	N.D.	N.D.	1 / 0.166[a]	0
(DX.64-69 × B6.P9$^{Hu/Hu}$) × B6[c]	369	N.D.	N.D.	N.D.	N.D.	0

[a] The recombination rate (cM/Mb) was calculated from the number of recombination events (*N*) and the number of BC1 animals tested (*n*) using the length (L) of a specific region on the X chromosome.

[b] Microsatellite PCR primer sequences used for genotyping are listed in Table S1.

[c] The B6.*Prdm9*$^{Hu/Hu}$ mouse strain carries *Prdm9*$^{Hu/Hu}$ on a B6 background, which was engineered by replacing the PRDM9^{B6} zinc-finger array with the human "B-allele" zinc finger array (Davies *et al.* 2016). B6.*Prdm9*$^{Hu/Hu}$ was crossed with B6.DX.64-69, and the female progeny was backcrossed with B6 males.

derived from this backcross carried only 4.34 Mb of the PWD sequence (Chr X: 64.87–69.21 Mb; mouse genome assembly GRCm38.p6) (Figure 1A). However, not a single recombination occurred in the *Hstx2* locus tracked by markers at Chr X: 65.10 and 69.08 Mb (Table 1). In the second backcross experiment, the B6.DX.51-69 subconsomic, which carries PWD sequence in the interval 51–69 Mb was used, but again no recombinant among 111 BC1 animals was found within the *Hstx2* locus. Finally, in an attempt to change the pattern of the recombination hotspots, the B6.*Prdm9*^{Hu} strain carrying the "humanized" PRDM9 with ZnF array from the human PRDM9^{A} allele (Davies *et al.* 2016) was used in (B6.*Prdm9*^{Hu} × B6.DX.64-69) × B6 backcross. No recombinant was found within the *Hstx2* locus among 369 BC1 animals. The absence of crossovers could occur due to the lack or inaccessibility of PRDM9 binding sites, the failure of SPO11 protein to target these sites and induce DNA DSBs, or because the repair of such DSBs is implemented exclusively by noncrossovers. The available data on female B6 meiosis (Brick *et al.* 2018) showed reduced occurrence of PRDM9-dependent H3K4me3 hotspots and absence of DMC1 hotspots within the *Hstx2* locus (Figure 2), suggesting the virtual disappearance of SPO11-generated DNA DSBs as a mechanism of recombination suppression. Remarkably, in male meiosis the strong suppression of DMC1 hotspots [data from Davies *et al.* (2016)] over the *Hstx2* locus observed in (PWD × B6) and (B6 × PWD) reciprocal F_1 hybrids was attenuated in PWD and B6 parental strains (Figure S1). To conclude, no recombinant in the *Hstx2* region was found among 648 BC1 mice, although 15 recombinants would be expected ($P = 2.495 \times 10^{-7}$, binomial test) based on the 0.526 cM/Mb mean recombination rate in the adjacent Chr X: 7.36–65.10 Mb proximal region. The recombination cold spot overlaps with the interval of low PRDM9 histone methyltransferase activity and strong suppression of DNA DSB hotspots.

Targeting homologous recombination to Hstx2 by CRISPR/Cas9

Because the *Hstx2* locus behaved as a cold spot of recombination, we attempted to bring the recombination machinery to this region by means of Cas9 endonuclease-induced DSBs. Two transgenic lines were prepared, the first carrying Cas9 endonuclease under the control of SPO11 genomic region to ensure exclusive expression of Cas9 at early prophase I of meiosis. The second transgenic strain was generated with the U6-promoter driven CRISPR cassette targeted to three sites within the *Hstx2* locus (see *Materials and Methods*). Next, the double transgenic F_1 females (B6.DX.1s.TgSPO11-Cas9 × B6.TgCRISPR-*Hstx2*) were mated to B6 males to generate the BC1 population. This approach allows the generation of targeted DSB by means of a transgene that can be removed through selective breeding in a B6 backcross design. We found that double transgenic F_1 females yielded a 15-fold higher frequency of recombination in the interval spanning 64.8-65.1 Mb immediately adjacent to the *Hstx2* locus (10 recombinants in 181 BC1 offspring, 18.42 cM/Mb) compared to previous classical backcrosses (one recombination event in 279 BC1 offspring, 1.19 cM/Mb). However, only one homologous recombination event inside the *Hstx2* locus was detected, giving rise to congenic strain B6.PWD-Chr X.66-69 (abbreviated B6.DX.66-69). The new congenic restricts the PWD sequence on Chr X to 2.70 Mb in the 66.51–69.21 Mb interval. Admittedly, all these recombinants occurred within the range bracketed by the guide RNAs but at some distance away from the sites targeted. At this point, we have not determined what may have caused the increase in recombination rate close to but not involving the targeted sites.

Phenotypes of newly defined Hstx1, Hstx2, and Meir1 loci

Hstx1 fertility phenotype: To check the *Hstx1* phenotype the fertility parameters of B6.DX.64-69 and B6.DX66-69 congenic males carrying the shortened 4.34 Mb (Chr X: 64.87–69.21 Mb) and 2.70 Mb (Chr X: 66.51–69.21 Mb) of PWD sequence were compared to B6.DX.1 and B6.DX.1s males carrying 64.9 and 69.2 Mb of proximal PWD sequence (Figure 1, A and B). Both shortened intervals of the PWD sequence reduced testes weight ($P < 0.05$, *t*-test) and caused higher frequency of morphologically malformed sperm heads compared to B6.DX.1 ($P < 0.01$, *t*-test, Figure 1B). However, compared to B6.DX.1s, the level of teratozoospermia

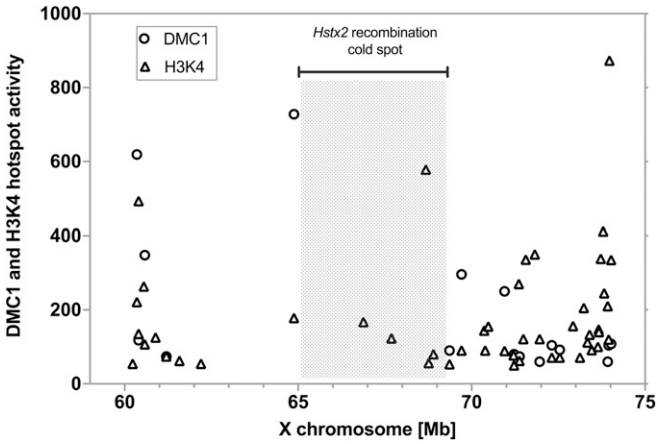

Figure 2 Activity of PRDM9-dependent H3K4 methylation and DMC1-marked DNA DSBs in female meiosis. The DMC1 and H3K4me3 hotspots plotted within the *Hstx2* locus and the adjacent regions of chromosome X (mm10 genome). The strong DMC1 hotspots coupled with H3K4 methylation lie outside the *Hstx2* region (shaded), which contains only H3K4 methylation marks. Data extracted from Brick *et al.* (2018); visualized are hotspots with activity >50.

controlled by the 4.34 and 2.70 Mb stretches of PWD sequence was significantly lower (40.8% *vs.* 69%, $P < 0.01$, *t*-test, Figure 1B). Thus, some additional genetic information proximal to the Chr X: 64.87–69.21 Mb interval is necessary to fully reconstruct the *Hstx1* phenotype.

***Hstx2* fertility and meiotic chromosome asynapsis phenotypes:** To verify the presence of *Hstx2* in the newly derived congenic strains, testes weight and sperm count were compared in F_1 hybrid males from crosses of PWD males and B6.DX.1, B6.DX.1s, B6.DX.64-69, and B6.DX66-69 females. The quasi-fertile phenotype of (B6.DX.1 × PWD) F_1 hybrids contrasted with full sterility of the remaining three types of hybrids as shown by low testes weight ($P < 0.0001$, *t*-test) and sperm count ($P < 0.0001$, *t*-test, Figure 1C). Thus in contrast to the *Hstx1* locus, the shortest version of *Hstx2* (Chr X: 66.51–69.21 Mb) was necessary as well as sufficient to fully reconstruct the (PWD × B6) F_1 male hybrid sterility phenotype.

Recently, we have found out that meiotic asynapsis of homeologous chromosomes (homologs from different subspecies) in (PWD × B6) F_1 hybrids depends on their subspecific origin and can be abolished by introduction a short stretches (27 Mb or more) of consubspecific homology into a given chromosome pair (Gregorova *et al.* 2018). Contrary to this chromosome-autonomous *cis*-control, the substitution of the $Hstx2^{PWD}$ allele for $Hstx2^{B6}$ in (B6 × PWD) F_1 hybrids significantly reduces meiotic asynapsis *in trans*, while the $Prdm9^{PWD}/Prdm9^{B6}$ genotype remains the same as in sterile hybrids (Bhattacharyya *et al.* 2014). To evaluate meiotic chromosome synapsis we visualized the axial elements of partially or fully asynapsed chromosomes by co-immunostaining of HORMA domain-containing protein-2, HORMAD2 (Wojtasz *et al.* 2012) and synaptonemal complex protein 3, SYCP3, in pachynemas of F_1 hybrids carrying different intervals of X^{PWD} (Figure 3). The highest proportion, 85.3 ± 1.3%, of pachynemas affected by asynapsis was observed in the (PWD × B6) F_1 hybrid males with intact X^{PWD} chromosome. The frequencies of pachynemas with asynapsis rates 78.9 ± 1.4%, 70.5 ± 8.6%, and 70.49% in three subconsomic F_1 hybrids (B6.DX.1s × PWD) F_1, (B6.DX.64-69 × PWD) F_1, and (B6.DX66-69 × PWD) F_1 did not differ from each other, but were significantly lower than in (PWD × B6) F_1s (Figure 3A). Importantly, the X^{B6} chromosome in (B6 × PWD) F_1 did not completely eliminate the *Prdm9* controlled asynapsis, which reached 38.9 ± 5.2% in (B6 × PWD) F_1 hybrid males (Figure 3A). It appears that in (B6 × PWD) F_1 hybrid genomic background this level of asynapsis rate could indicate a threshold of azoospermia because (B6 × PWD) F_1 hybrid males with <40% asynapsis rate showed 7.2 ± 4.2 × 10^6 epididymal sperm count, while males of the same genotype with >40% asynapsis were virtually azoospermic (0.12 ± 0.1 × 10^6 sperm count).

To conclude, ~three-quarters of the *Hstx2* effect on *Prdm9*-controlled asynapsis rate is preserved in the newly reduced 2.70 Mb PWD sequence version (Chr X: 66.51–69.21 Mb); the remaining effect either maps elsewhere on the X chromosome or is the consequence of a hypothetical position effect of the *M. m. domesticus* genome on the introgressed *M. m. musculus* sequence.

***Meir1* control of global meiotic recombination rate:** The *Meir1* was localized in the *Hstx2* interval as the strongest transgressive modifier of the meiotic recombination rate in B6.DX.1s males. The $Meir1^{PWD}$ coming from the high-recombination rate PWD strain lowered crossover frequency in a transgressive manner when introgressed into the B6 genome (Balcova *et al.* 2016). The crossover frequency determined by counting the MLH1 foci per pachytene spermatocyte revealed that both the 4.34 and 2.70 Mb PWD interval reduced recombination compared to B6 and B6.DX.1, thus behaving as *Meir1*, but the reduction did not reach the level seen in B6.DX.1s (Figure 4). We conclude that similarly as in the case of the newly defined *Hstx1* locus some additional genetic information in the proximal PWD sequence besides the 2.70 Mb interval is necessary to fully reconstruct the *Meir1* phenotype (Figure 4, A and B).

Optical mapping of intersubspecific structural variation within and outside the Hstx2 locus

One possible cause of the recombination cold spot overlapping the *Hstx2* locus could be a structural rearrangement, typically an inversion that prevents recovery of viable recombinants. Such structural variants acting as recombination suppressors often enforce reproductive isolation between species, especially when situated on sex chromosomes (Kirkpatrick 2010; Hooper *et al.* 2018). To elucidate the physical structure of *Hstx2* locus we analyzed the region by optical mapping using the Bionano Saphyr platform, a further development of the technique described by (Chan *et al.* (2018)). As a proof of

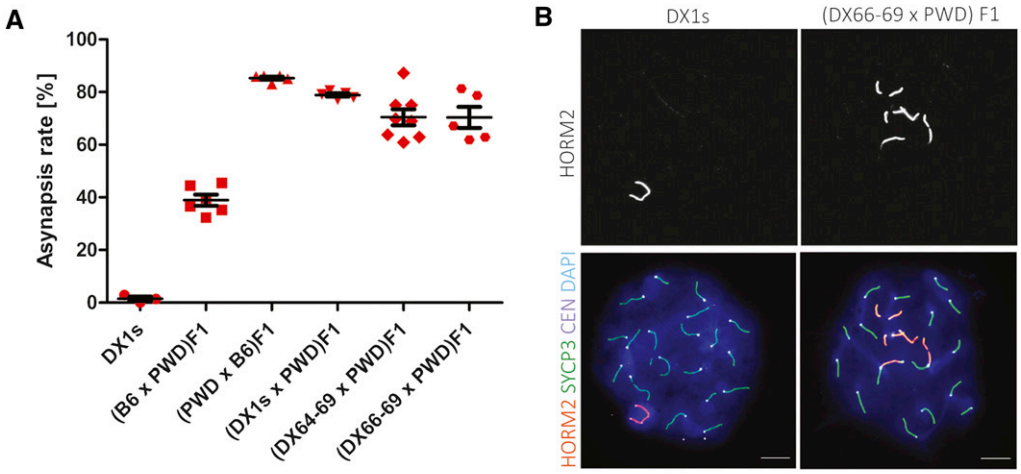

C

strain	DX1s	(B6 x PWD)F1	(PWD x B6)F1	(DX1s x PWD)F1	(DX64-69 x PWD)F1	(DX66-69 x PWD)F1
DX1s	X	< 0.0001	< 0.0001	< 0.0001	< 0.0001	< 0.0001
(B6 x PWD)F1		X	< 0.0001	< 0.0001	< 0.0001	0.0004
(PWD x B6)F1			X	0.0001	0.0016	0.0201
(DX1s x PWD)F1				X	0.0274	0.1015
(DX64-69 x PWD)F1					X	0.9880
(DX66-69 x PWD)F1						X

Figure 3 Pivotal role of the *Hstx2* locus in the pachytene asynapsis rate of male F_1 hybrids. (A) The mean values of asynapsis rate (± SD) in F_1 and B6.DX.1s hybrid males carrying different portions of X^{PWD}. Autosomal asynapsis (frequency of pachynemas with one or more asynapsed autosomes) was examined in 5–8 animals of a given genotype, scoring at least 50 pachytene nuclei per one male. (B) Representative immunofluorescence micrographs show the HORMAD2-positive XY pair in a pachytene spermatocyte of B6.DX.1s congenic male and asynapsed autosomes in (DX.66-69 × PWD) F_1 hybrids. Asynapsed chromosome axes are immunostained by HORMAD2 antibody. SYCP3 visualizes lateral elements of synaptonemal complexes. CEN labels centromeric heterochromatin, and DAPI labels nuclear DNA. Bar, 10 μm. (C) Comparisons of the asynapsis rates between individual animal groups were performed by two-tailed *t*-test, and the *P*-values are displayed in the table.

concept, we examined the *Hstx2*^{PWD} *M. m. musculus* introgression in the *M. m. domesticus* Chr X^{B6}. Indeed, the 64–69 Mb interval of Chr X was easily recognizable in two optical maps from biological replicas of B6.DX.64-69 mice when matched with the reference B6/J *in silico* map and with the map of a female from the C57BL/6Crl substrain. The structure of the 64–69 Mb interval of Chr X matched most closely the PWD and PWK optical maps, while the flanking intervals matched the B6 optical map. (Figure 5, A–C). To inquire into the overall divergence of the *Hstx2* locus as a possible cause of recombination suppression, optical maps of the region of the same size outside the recombination cold spot (Chr X: 59.6–64.0 Mb) was compared to the *Hstx2* region (Chr X: 64.8–69.2 Mb) from four mouse strains (B6/N, B6.DX.64-69, PWD, and PWK) by alignment to the mm10 *in silico* reference (Table 2). Although only 0.08% of the control locus sequence was involved in deletions or insertions in B6/N and B6.DX.64-69, the same 4.3 Mb control interval included 6.92% of deleted or inserted sequence in PWD and PWK. In comparison, the *Hstx2* locus (Chr X: 64.8–69.2 Mb) displayed 2 insertions of 8.7 kb and no deletion in the B6/N, representing 0.02% of the sequence, while 4.71% of sequence was either inserted or deleted in B6.DX.64-69, 4.58% in PWD, and 5.90% in PWK. Intraspecific comparison of the same *Hstx2* interval yielded 1.11% and 2.40% of sequence involved in PWK and PWD specific inversions and deletions. To conclude, the overall structural dissimilarity is surprisingly high between *M. m. musculus* and *M. m. domesticus* subspecies, but unlikely to explain the *Hstx2* recombination cold spot.

Fine-scale screen for the Hstx2-specific structural variants

A structural variant within the *Hstx2* locus could be a marker of the *Hstx2* candidate gene. Thus we screened for PWD-specific structural variations within the *Hstx2* locus because the *Hstx2* alleles differ between *M. m. musculus* PWK and PWD and *M. m. domesticus* B6 mice (Flachs *et al.* 2014). We first aligned *de novo* maps of B6.DX.64-69, PWD, PWK, and C57BL/6Crl to the C57BL6/J *in silico* reference, generating a quadruple assembly (Figure 5). We then screened for structural variants that occur in B6.DX.64-69 and PWD but not in C57BL/6Crl or PWK. This had to be done semimanually, as due to the large genetic divergence in this interval, relying only on Bionano's automated algorithms was insufficient. A fine-scale characterization of the refined *Hstx2* interval by manual label matching revealed three high-confidence structural variants. The first locus, found between Chr X positions 66.756–66.797 Mb, contains two long terminal repeats (LTRs) in the B6 reference. While PWD and PWK both possess a 4.7 kb deletion of the first LTR, the second LTR locus downstream harbors a 3.1 kb deletion in PWD, also deleting miRNA *Mir883b*. In contrast, PWK shows a large overlapping 45.0 kb insertion (Figure 6A). The second significant structural variation is located between chromosomal positions 66.819–66.840 Mb, and includes the *Mir465* cluster, which appears differentially duplicated in PWK and PWD (Figure 6B). In PWD we observed an insertion of 22.9 ± 4 kb, while the PWK map revealed a shorter insertion of only 16.3 kb. Previously, we found overexpression of the *Hstx2*

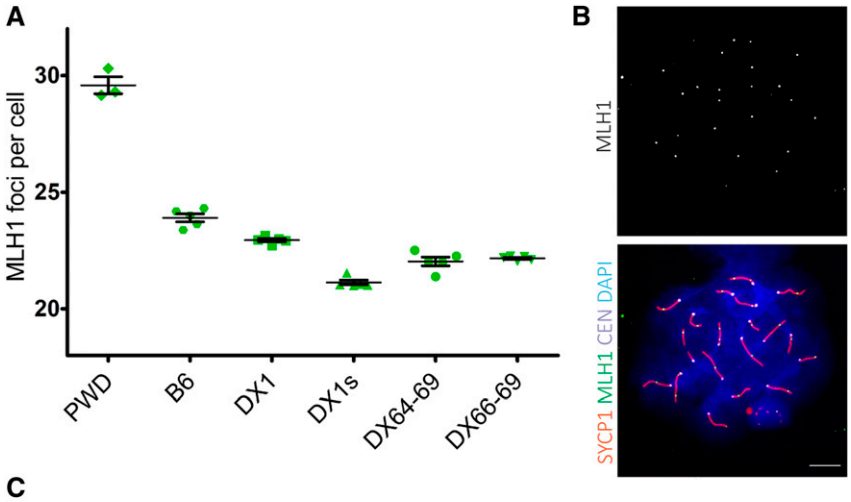

C

	PWD	B6	DX1	DX1s	DX64-69	DX66-69
PWD	X	< 0.0001	< 0.0001	< 0.0001	< 0.0001	< 0.0001
B6		X	0.0009	< 0.0001	< 0.0001	< 0.0001
DX1			X	< 0.0001	0.0019	< 0.0001
DX1s				X	0.0029	< 0.0001
DX64-69					X	0.5117
DX66-69						X

Figure 4 Transgressive effect of the *Hstx2*^{PWD} allele on crossover rate. (A) The mean crossover rate values (± SD) are shown for the subconsomic and congenic males carrying different portions of the chromosome X^{PWD} on the B6 genetic background. (B) Representative immunofluorescence micrograph visualizing MLH1 foci (green), synaptonemal complex protein 1, SYCP1 (red), centromeric proteins, CEN (white), and nuclear DNA (blue) in the B6.DX.1s late pachytene spermatocyte. Bar, 10 μm. (C) Summary of comparisons of the recombination rates between individual animal groups are shown in the table as *P*-values analyzed by unpaired two-tailed *t*-test.

miRNA cluster, particularly of *Mir465* in sterile hybrids (Bhattacharyya *et al.* 2014). A differential duplication could therefore harbor subspecies-specific differences in *Mir465* expression, which may confer dosage effects on the regulation of downstream target genes.

The third is a homozygous deletion of 4574 ± 9 bp situated at Chr X: 67,787,047–67,795,903. However, this deletion neither interrupts nor deletes any known gene, mRNA/miRNA sites, or transcripts in the available testis transcriptomics data sets (Margolin *et al.* 2014; Harr *et al.* 2016; Jung *et al.* 2019) (Figure 6C). This structural variant is thus an unlikely candidate for harboring *Hstx2*.

Probing Fmr1nb as an Hstx2 candidate gene

The newly reduced *Hstx2* genomic interval incorporates eight protein-coding genes, of which the Fmr1 neighbor (*Fmr1nb*) appeared as the best potential candidate for the *Hstx2* gene.

The priority was based on *Fmr1nb* expression at early meiotic prophase I (Margolin *et al.* 2014; Ball *et al.* 2016; Jung *et al.* 2019; Ernst *et al.* 2019) and two nonsynonymous single nucleotide polymorphisms between PWD and B6 parental strains (Table S5). We confirmed almost exclusive expression of *Fmr1nb* in the testis, with only traces in the spleen and heart (Figure S2A) and found 2.5-fold higher expression in sterile (PWD × B6) F_1 adult testis compared to the PWD and B6 parental strains ($P < 0.001$, $P < 0.001$; *t*-test) (Figure S2B). A continuous increase of the mRNA level of *Fmr1nb* was found in juvenile males at 10, 12, 14, and 20 days of postnatal development; however, all three genotypes showed a similar expression pattern (Figure S2C). The predicted structure of the FMR1NB protein (Figure S3) consists of two cytosolic N- and C-terminal domains, two transmembrane domains, and an extracellular part containing a P-type trefoil domain. The mouse *Fmr1nb* transcripts occur in three splice variants (ENSMUSG00000062170.12, ENSEMBL) corresponding to three isoforms of FMR1NB protein (Q80ZA7, UniProt) comprising 238, 192, and 166 amino acids, respectively. We found that in the testis, the most abundant is isoform 3 (Figure S3), made up of 166 amino acids. It lacks the complete P-type trefoil domain and most of the extracellular domain. Two FMR1NB nonsynonymous substitutions create exchanges of 31 arginine^{PWD} for threonine^{B6} and 162 leucine^{PWD} for isoleucine^{B6}.

Using fluorescence immunolabeling, we detected the FMR1NB protein on histological sections of the testis of adult B6 males in the cytoplasm and spermatocyte cell membranes. The strongest FMR1NB expression was found at the leptotene and zygotene stages of the first meiotic prophase. The signal decreased in pachynemas, and disappeared in the round and elongated spermatids (Figure S2D).

Fertility phenotypes of Fmr1nb null mutants: To test the effect of the *Fmr1nb* null allele on the *Hstx1/2* phenotypes, two mouse lines carrying *Fmr1nb* deletion mutants were generated by TALEN nuclease method (see *Material and Methods* and Figure 7A). The coisogenic mouse line B6.*Fmr1nb*^{em1ForeJ} carried 236 bp deletion within the first exon and B6.DX.1s.*Fmr1nb*^{em2ForeJ} displayed a 19 bp deletion over

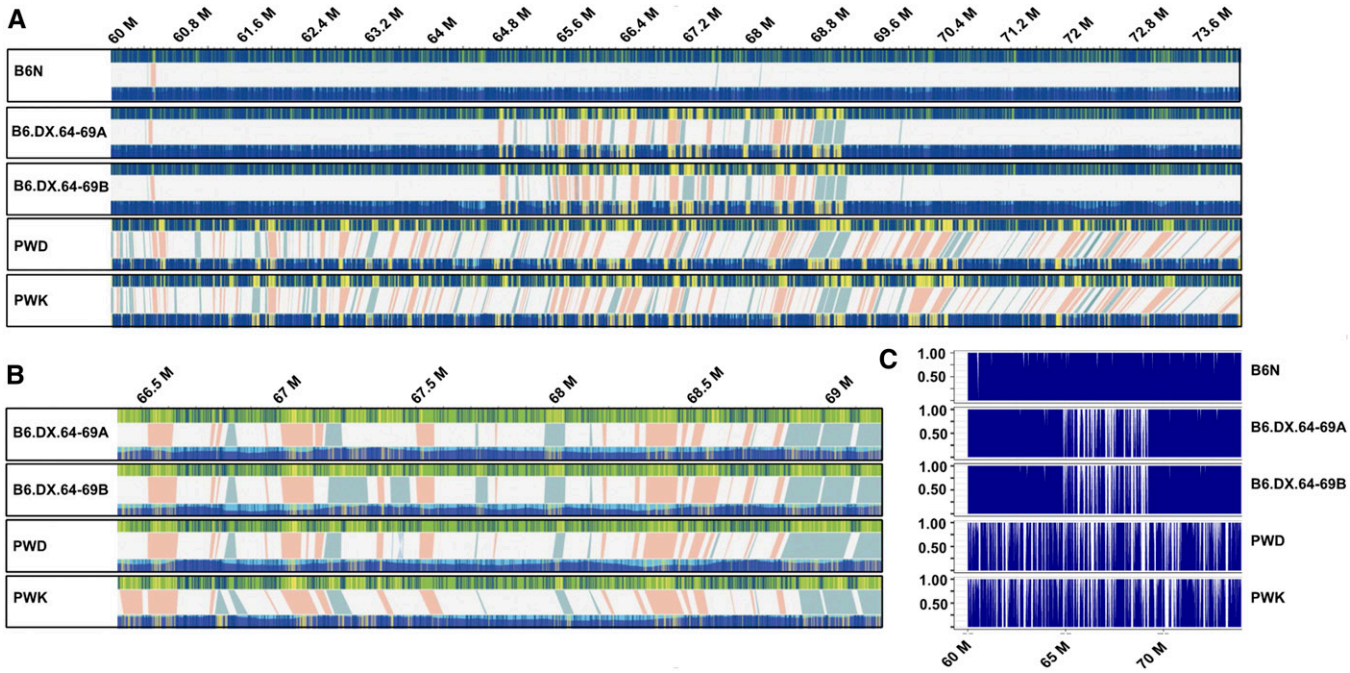

Figure 5 Structural variants (SVs) in the *Hstx2* locus and in flanking regions. Each box contains a comparative analysis of a *de-novo* optical map (bottom), and the mm10 *in-silico* reference B6 map (top) of a given individual. (A) Five maps of B6N, B6.DX.64-69A, B6.DX.64-69B, PWD, and PWK spanning Chr X 60–74 Mb (images extracted from Bionano Solve version 3.3_10252018 at maximum resolution). At this overview, individually-labeled restriction sites are not visible. However, matching intervals appear blue on both the reference and *de novo* map, as labeled restriction sites matching their predicted position in the reference are depicted as blue lines. In contrast, labels found in either the reference or *de novo* map, but not both, are marked by yellow lines. Therefore, clusters of mismatched labels become visible as yellow blocks. Label patterns are used to predict SVs by the Bionano Solve software. Putative SVs are depicted as shaded areas, connecting the upper reference and lower *de novo* map. Light red areas represent putative deletions, where labels present in the *in silico* reference, are absent in the *de novo* map. In contrast, light blue shaded areas depict putative insertions, where additional labels were found in the *de novo* map, but not the *in silico* reference. (B) The same optical maps for B6.DX.64-69A, B6.DX.64-69B, PWD, and PWK, zoomed in to *Hstx2* position X: 66.51–69.21 Mb, which is an apparent recombination cold spot. All putative SVs are shown at higher resolution, with deletions in red and insertions in blue. Neither large inversions nor translocations have been predicted for this interval. (C) To quantify the number of labels matching between *in silico* map and each of the five *de novo* maps, we counted all labels across Chr X 60–74 M (see Table 2). Proportions of matching labels are plotted per 10 kb nonoverlapping window.

the ATG start codon (these lines are henceforth called B6.*Fmr1nb*$^{-}$ and B6.DX.1s.*Fmr1nb*$^{-}$). The *Fmr1nb* mRNA was detectable by quantitative Reverse Transcription-PCR in both transgenic lines as expected because the transcription start site was not affected (not shown). Three FMR1NB isoforms were identified by Western blotting in males carrying *Fmr1nb*^{B6} and *Fmr1nb*^{PWD} alleles, while the FMR1NB protein was missing in the mutant testes (Figure 7B). Intriguingly, the most truncated isoform 3 of FMR1NB was expressed most strongly in the testes of all four genotypes, whereas the longer isoforms iso-1 and iso-2 showed low expression in B6 and (B6 × PWD) F_1, and even lower in (PWD × B6) F_1 sterile hybrids and no expression in PWD and B6.DX.1s (Figure 7B). Immunohistochemistry of testes of adult wild type males showed high expression of FMR1NB in spermatogenic cells in early stages of meiotic prophase I. The protein was missing in histological sections from the B6.DX.1s.*Fmr1nb*$^{-}$ knockout males (Figure 7C), but the overall composition of testicular tubules did not show any apparent changes (Figure 7D).

The *Fmr1nb*$^{-}$ males bred successfully, but their mean litter size was significantly lower than litter size of males carrying the wild-type alleles (Figure S4). The B6.*Fmr1nb*$^{-}$ and B6 males did not differ significantly in the testes weight (165.8 ± 22.2 *vs.* 180 ± 16.8 mg; $P = 0.133$, *t*-test) or in the sperm count (54.5 ± 18.2 × 10^6 *vs.* 73.3 ± 17.5 × 10^6; $P = 0.073$, *t*-test) (Figure S5, A and B), but B6.*Fmr1nb*$^{-}$ displayed a significantly higher proportion of malformed sperm heads (32.9 ± 8.6 *vs.* 19.8 ± 4.2%; $P < 0.05$, *t*-test) (Figure S5C).

The effect of the *Fmr1nb*^{PWD} null allele was stronger on the B6.DX.1s genetic background. Testes weight of the B6.DX.1s.*Fmr1nb*$^{-}$ males was significantly lower than in B6.DX.1s (148.1± 16.1 *vs.* 171.9 ± 8.8; $P < 0.001$, *t*-test) (Figure S5D) and the sperm count was lower in B6.DX.1s.*Fmr1nb*$^{-}$ than in B6.DX.1s males (44.2 ± 12.8 *vs.* 53.5 ± 10 × 10^6; $P < 0.05$, *t*-test) (Figure S5E). Furthermore, the B6.DX.1s.*Fmr1nb*$^{-}$ males showed significantly higher proportion of malformed sperm heads than B6.DX.1s control males (76.9 ± 8 *vs.* 69 ± 7.3%; $P < 0.05$, *t*-test) (Figure S5F). The frequency of apoptotic cells in seminiferous tubules assessed by fluorescence TUNEL labeling of histological sections was higher in the B6.DX.1s.*Fmr1nb*$^{-}$ males (3.36 ± 0.23) compared to B6.DX.1s males (1.46 ± 0.39, $P < 0.005$; Figure S6, A and B).

Table 2 Insertions and deletions in the *Hstx2* locus compared to control intervals on chromosomes X

Mouse strain	Control Chr X coordinates (Mb)	Insertions, *n* /(kb)	Deletions, *n* /(kb)	*Hstx2 locus* coordinates (Mb)	Insertions, *n* /(kb)	Deletions. *n* /(kb)
B6.N	Chr X: 59.6–64.0	1 / 0.9	1 / 2.8	Chr X: 64.8–69.2	2 / 8.8	0
B6.DX64-69_A	Chr X: 59.6–64.0	1 / 0.9	1 / 2.6	Chr X: 64.8–69.2	14 / 94.1	26 / 116.3
B6.DX64-69_B	Chr X: 59.6–64.0	1 / 0.9	1 / 2.8	Chr X: 64.8–69.2	15 / 92.6	26 / 111.6
PWD	Chr X: 59.6–64.0	22 / 105.7	21 / 174.4	Chr X: 64.8–69.2	12 / 85.8	29 / 116.4
PWK	Chr X: 59.6–64.0	21 / 113.4	24 / 192.1	Chr X: 64.8–69.2	14 / 140.3	26 / 119.4

Optical maps over the *Hstx2* region (Chr X: 64.8–69.2 Mb) and the control *Hstx2*-adjacent interval of the same size (Chr X: 59.6–64.0Mb) from five mouse genome DNA samples, representing four mouse strains, were generated and aligned to the mm10 *in silico* reference map. Coordinates are given with respect to the position in the mouse genome reference mm10 (Mb), *n* / (kb) numbers and cumulative sizes of structural variants within the intervals of the same extent in the X chromosome.

To inquire whether *Fmr1nb* interacts with the *Hstx2* phenotype, the hybrid males were analyzed for the testes weight and sperm count. Neither the $Fmr1nb^{B6}$ nor $Fmr1nb^{PWD}$ null allele rescued hybrid sterility; on the contrary, the $Fmr1nb^{PWD}$ null allele in (B6.DX.1s.$Fmr1nb^{-}$ × PWD) F_1 hybrid males significantly reduced the testes weight when compared to (B6.DX.1s × PWD) F_1 control males (59.3 ± 4.1, and 67.7 ± 3.5 mg; $P < 0.001$, *t*-test, see Table S6).

To conclude, the *Fmr1nb* on the B6 genetic background is necessary for the normal course of spermiogenesis, with stronger effects in the PWD context of B6.DX.1s *Fmr1nb* congenic males. In intersubspecific F_1 hybrids, however, the absence of FMR1NB modifies neither the intrameiotic arrest nor hybrid sterility.

Discussion

Two-gene architecture of hybrid sterility

Our model of hybrid sterility based on (PWD × B6) F_1 hybrids is composed of three main components: the *Prdm9* gene, subspecific divergence of homeologous autosomes, and the *Hstx2* locus. It differs in its simplicity from the complex genetic control reported by other studies using the same combination of house mouse subspecies (Tucker *et al.* 1992; Payseur *et al.* 2004; Macholán *et al.* 2007, 2011; Duvaux *et al.* 2011; Janoušek *et al.* 2012; Turner *et al.* 2012).

PRDM9 protein activates a high number of asymmetric DNA DSBs in prophase I of (PWD × B6) F_1 primary spermatocytes, so that $PRDM9^{B6}$-determined hotspots occur mostly on the PWD chromosome and *vice versa* (Davies *et al.* 2016; Smagulova *et al.* 2016; Hinch *et al.* 2019). The main reason of hotspot asymmetry is the evolutionary erosion of the PRDM9 DNA binding sites (Baker *et al.* 2015). The predominant role of PRDM9-induced DSB asymmetry in this model of hybrid sterility was emphasized by complete recovery of spermatogenesis and fertility of the (PWD × B6) F_1 hybrids when the zinc-finger array of $PRDM9^{B6}$ was replaced with the human orthologous sequence (Davies *et al.* 2016). The hotspot erosion and meiotic failure disappeared because $PRDM9^{Hum}$, in contrast to $PRDM9^{B6}$, has never before been in contact with mouse genome. Full recovery can be also achieved by homozygosity for the $Prdm9^{PWD}$ allele (Dzur-Gejdosova *et al.* 2012).

The importance of *cis*-interaction between homeologous chromosomes was shown in intersubspecific backcross males where asymmetry disappeared in conspecific autosomal intervals (PWD/PWD or B6/B6) (Gregorova *et al.* 2018), which initially had been misinterpreted as multiple hybrid sterility QTL (Dzur-Gejdosova *et al.* 2012). The major meiotic consequences of DSB hotspot asymmetry include persistent DNA DSBs and meiotic asynapsis, both leading to apoptosis (Davies *et al.* 2016; Gregorova *et al.* 2018; Wang *et al.* 2018).

The role of *Hstx2* is apparent from attenuated manifestation of the *Prdm9*-driven asynapsis phenotype and subsequent meiotic arrest in the reciprocal (B6 × PWD) F_1 hybrids. Previously we excluded mitochondrial inheritance, the Y chromosome, and genomic imprinting as a cause and identified the *Hstx2* locus on Chr X to be the culprit (Dzur-Gejdosova *et al.* 2012; Bhattacharyya *et al.* 2014). We have not yet identified the genetic factor behind the *Hstx2* locus, so it is difficult to guess why the same pair of homeologous autosomes with the same ratio of asymmetric/novel DMC1 hotspots (Davies *et al.* 2016; Smagulova *et al.* 2016) differs so strongly in DSB repair and meiotic synapsis in the reciprocal hybrids. Three main options can be considered: *Hstx2* could extend the time window necessary to accomplish the repair of mutated PRDM9 binding sites, it could reduce the sensitivity of putative mismatch repair anticrossover activity to sequence heterology (Spies and Fishel 2015), or it may facilitate the switch of repair partner bias by sister chromatid homologous recombination (Garcia-Muse *et al.* 2019).

A recombination cold spot overlaps the Hstx2 locus

Empirical results from rabbits and mice strongly indicate that genomic regions with suppressed recombination are more differentiated and tend to accumulate reproductive isolation genes (Nachman and Payseur 2012). Ortiz-Barrientos *et al.* (2016) predicted that "...regions of low recombination will tend to harbor genes for various forms of reproductive isolation, as well as modifiers of recombination during the early stages of speciation..." Indeed, the hybrid sterility genetic locus *Hstx2* meets both of these predictions since it is situated in a recombination cold spot and carries *Meir1*, an underdominant modifier of meiotic recombination rate. Moreover, *Hstx2* operates at early stage of speciation when reproductive isolation of *Mus musculus* subspecies is still incomplete. In an attempt to reduce the size of the *Hstx2* locus by genetic

Figure 6 Detailed examination of polymorphic structural variation in the *Hstx2* locus. Blue vertical lines represent perfect matches to the predicted B6 *in silico* optical map (mm10), while yellow vertical lines are additional detected labels that do not match the reference. Structural variants (SVs) between the B6 reference and respective *de novo* optical map are depicted as colored triangles, deletions in orange, and insertions in blue. At the bottom of the panel, the ENSEMBL tracks for LTRs and genes are shown, with vertical lines representing the interval affected by the SVs depicted in the top panel. (A) The optical maps zoomed to interval at Chr X: 66.75–66.80 Mb, revealing a polymorphic LTR region. Here, PWD possesses two deletions while PWK displays only one deletion, plus an insertion. (B) The optical map zoomed in at interval Chr X: 66.76–66.84 Mb. PWD and PWK both bear insertions, which duplicate the locus containing the Mir465 miRNA cluster, compared to the orthologous region in B6J. These insertions are polymorphic between the two *M. m. musculus* chromosomes, spanning only 16.2 kb in PWK but 23.3 kb in PWD. (C) Optical map zoomed in at interval Chr X: 67.75–67.81 Mb, which possesses a deletion in PWD only. However, the deletion does not appear to disrupt any known gene.

recombination, we used three genetic backcrosses, one of them employing the "humanized" *Prdm9*^{Hu} allele known to determine a DSB hotspots landscape entirely different from the *Prdm9*^{dom2} allele. However, none of these crosses was able to break the 4.3 Mb cold spot. The only recombinant which reduced *Hstx2* to 2.7 Mb was obtained in a backcross where SPO11-driven Cas9 nuclease was targeted by CRISPR to *Hstx2* interval in female meiotic prophase. Because the recombination breakpoint lies outside the targeted sites and outside SPO11-oligo hotspots (Lange *et al.* 2016), the possibility that this unorthodox crossover arose by repairing a Cas9-generated DSB seems unlikely.

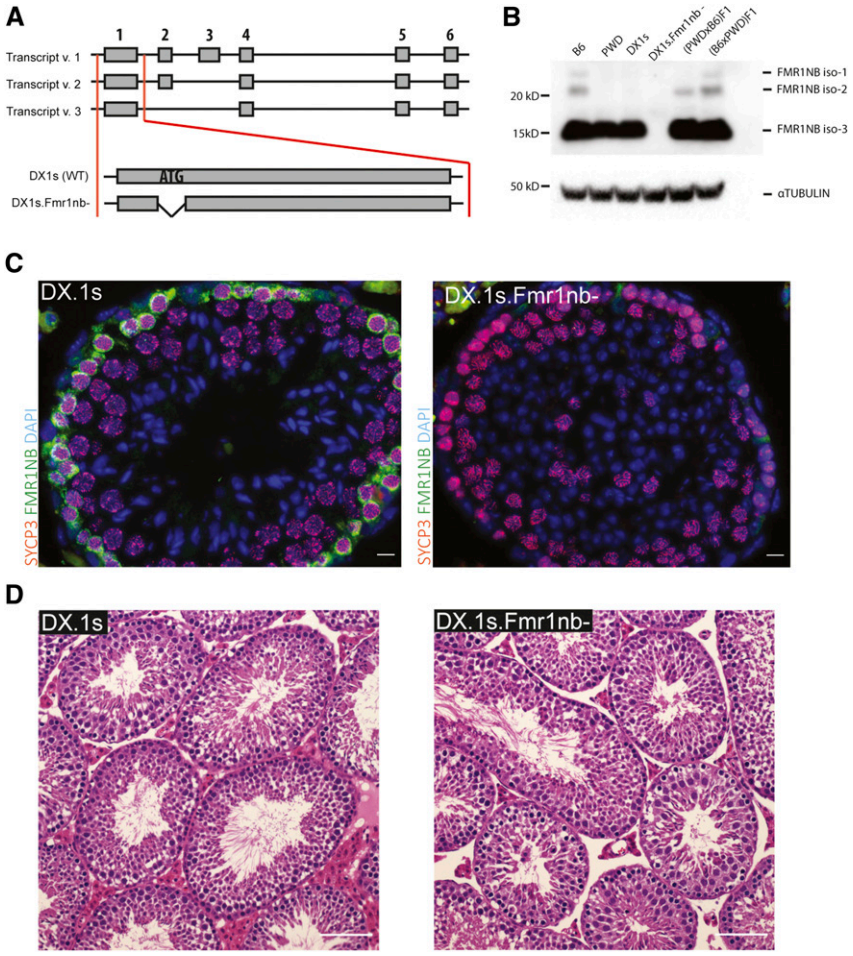

Figure 7 Generation of *Fmr1nb* null allele. (A) Transcript variants of *Fmr1nb* are shown, comprising six, five, and four exons. Deletion mutants of B6 and PWD alleles of *Fmr1nb* were generated by TALEN nuclease pair constructs targeted to the ATG start codon of *Fmr1nb* in C57BL/6N (B6N) laboratory strain and C57BL/6J-ChrX.1s$^{PWD/Ph}$ (B6.DX.1s) subconsomic strain, respectively. (B) FMR1NB protein levels in the testes of males of indicated genotypes were assessed by Western blot. None of the three isoforms of FMR1NB was detectable in the *Fmr1nb*-deficient strain. Loading control was alpha-tubulin. (C) Immunolabeling of FMR1NB and SYCP3 in histological sections of testis of B6.DX.1s and B6.DX.1s.*Fmr1nb*. *FMR1NB* is shown in green, *SYCP3* is shown in violet, and DAPI is shown in blue. Bar, 10 μm. (D) The histological sections of testes of the B6.DX.1s and B6.DX.1s.*Fmr1nb*$^{-}$ genotype stained with hematoxylin and eosin displayed no changes in morphology and occurrence of the meiotic cells. Bar, 100 μm.

The cold spots of recombination are often caused by heterozygosity for large structural variations, often inversions, and these "frozen" blocks can harbor genetic factors important for reproductive isolation (Coyne and Orr 2004; Fuller *et al.* 2018). In contrast to inversions, large copy number variants can be associated with closed chromatin and reduced gene expression in germ cells, suggesting a constitutive effect on recombination by altering chromatin structure (Morgan *et al.* 2017). A constitutive cold spot model seems to better fit to the *Hstx2* locus based on the low histone methyltransferase activity of PRDM9 and strong depression DNA DSB hotspots in the *Hstx2* region in female meiosis (Brick *et al.* 2018). The conclusion is also supported by recombination data from 73 sequenced inbred strains of the Collaborative Cross project (Collaborative Cross Consortium 2012; Srivastava *et al.* 2017). We found that none of the sequenced strains carries a single recombination event within the 8 Mb (Chr X: 61.8–70.3Mb) interval spanning *Hstx2*, while 9 and 10 recombinants occurred in the adjacent 8 and 6 Mb regions (http://csbio.unc.edu/CCstatus/index.py?run=CCV). In the Diversity Outbred project that used the same eight parental strains strong association between copy number variants regions and recombination cold spots was found (Morgan *et al.* 2017).

The present results based on optical mapping of a single genomic region indicate that genome-wide optical mapping can greatly contribute to elucidating the "fluidity" of noncoding sequences between related species as well as to clarify the greater differentiation of X chromosome compared to the autosomes (Hammer *et al.* 2008; Presgraves 2018). The optical mapping enabled unprecedentedly high resolution of the *Hstx2* locus physical map in the *M. m. musculus* (PWD) and *M. m. domesticus* (B6) genome, but did not provide evidence of an inversion that could explain the recombination cold spot. Provided that the *Hstx2* phenotype is associated with a structural variant, then it should be visible in the PWD sequence, but not in PWK or B6. Three such PWD-specific variants have been found, but only one of them, including a cluster of miRNA genes, can directly implicate functional consequences related to *Hstx2*. To conclude, these results together with the recombination data from the Collaborative Cross project show that the *Hstx2* locus is located within a constitutive recombination cold spot with the chromatin structure poorly accessible to the recombination machinery.

Hstx1 and Meir1 genetic factors located in the newly defined Hstx2 locus

The *Hstx1* was mapped on Chr X as a QTL common for several male fertility phenotypes following the transgression of Chr

X^{PWD} into the B6 genome. In the same experiment the suppression of recombination in the Chr X: 59.65–72.41 Mb interval (*DXMit140–DXMit199*) was noticed for the first time and the QTL for number of offspring, testes weight and sperm morphology was mapped to the interval near the *DXMit199* marker (Storchová *et al.* 2004). Later, the X-linked *Hstx2* locus controlling the early meiotic arrest in (PWD × B6) F_1 hybrids was localized in the same area (Bhattacharyya *et al.* 2014).

The effect of *Meir1* genetic factor on meiotic recombination is paralleled by the male-limited transgressive/underdominant effect of *Hstx2* on hybrid sterility, since the $Meir1^{PWD}$ allele of the high recombination rate PWD parent causes downregulation of crossover rate after introgression in the low recombination rate B6 strain. Thus the localization of *Meir1* within the *Hstx2* locus indicates a link between meiotic recombination and hybrid sterility (Balcova *et al.* 2016).

In the course of positional cloning of QTL in mice and other organisms, the QTL effect sometime weakens or even disappears with narrowing down the critical region. In most instances the weakening of QTL's effect was explained by several physically linked small effects (Flint *et al.* 2005). We have seen some weakening of all three genetic factors mapping to the 2.70 Mb interval, which can be explained in the same manner. Alternatively, an epigenetic positional *cis*-effect could be involved.

The role of the Fmr1 neighbor (Fmr1nb) gene in male fertility

In the present study, we selected the *Fmr1nb* gene as the most promising candidate of *Hstx2* based on its expression pattern during meiotic prophase I and two missense polymorphisms between PWD and B6 alleles. Although the role of *Fmr1nb* in male fertility was challenged in a study of 54 testis-expressed genes (Miyata *et al.* 2016), we showed that the *Fmr1nb* null allele induced apoptosis of spermatogenic cells, elevated the frequency of sperm head malformations and decreased sperm counts. A similar general function in cellular proliferation and apoptosis was described for human FMR1NB in glioma cells (Wu *et al.* 2018). The phenotype of *Fmr1nb* null mutants, in particular the occurrence of abnormal sperm heads mimics the *Hstx1* effect. However, since teratozoospermia is a common pathological phenotype with many possible causes, and given that the null allele of *Hstx1* does not eliminate fertility phenotype differences between B6.DX.1 and B6.DX.1s, we consider *Fmr1nb* an unlikely candidate for *Hstx1*. Moreover, since the lack of FMR1NB protein did not modulate the pachytene arrest in (PWD × B6) F_1 hybrids, we also do not consider *Fmr1nb* as candidate of *Hstx2*.

miRNA cluster variation within the Hstx2 locus

The *Hstx2* locus harbors an evolutionary conserved group of 12 testis specific miRNAs residing in two clusters of 19 and 3 miRNAs situated between *Slitrk2* and *Fmr1* protein coding genes. The conserved location of these miRNA clusters anchored between the two X-linked genes was reported in 12 mammalian species (Zhang *et al.* 2019). In spite of the interspecific variability in number of individual miRNA genes, the levels of testicular miRNAs are under regulatory constrains because depletion as well as overexpression of specific miRNA molecules or miRNA clusters can be deleterious for male fertility (Royo *et al.* 2015; Ota *et al.* 2019). The X-linked miRNAs are actively transcribed in spermatogonia and suppressed by meiotic sex chromosome inactivation in pachytene spermatocytes (Royo *et al.* 2010). Since mouse hybrid sterility is accompanied by PRDM9-controlled meiotic silencing of unsynapsed chromatin and consequent disturbance of meiotic sex chromosome inactivation (Bhattacharyya *et al.* 2013; Campbell *et al.* 2013; Larson *et al.* 2016), the uninhibited miRNA clusters could suppress genes necessary for meiosis, thus acting as "lethal mutants" contributing to meiotic arrest. Previously we have found overexpression in pachynemas of the miR-465 miRNA cluster in sterile (PWD × B6) F_1 compared to reciprocal, quasi-fertile (B6 × PWD) F_1 males (Bhattacharyya *et al.* 2013). Remarkably, this cluster is subjected to copy number variation between PWD, PWK, and B6 strains. Admittedly, until we identify the gene/sequence responsible for the *Hstx2* phenotype, such speculations have to be taken with a grain of salt. Indeed, in reciprocal crosses between the *M. m. musculus* STUS strain and B6, both reciprocal hybrid males were fully sterile, showing that in this particular cross the $Prdm9^{msc}$/$Prdm9^{dom2}$ hybrid sterility phenotype was not dependent on *Hstx2* allele (Bhattacharyya *et al.* 2013).

Summary

Early meiotic arrest of mouse intersubspecific hybrids depends on the interaction between the *Prdm9* gene and Hybrid sterility X2 (*Hstx2*) locus on chromosome X. Lustyk *et al.* conducted high-resolution genetic and physical mapping of the *Hstx2* locus, reduced it to 2.7 Mb interval within a constitutive recombination cold spot and found that the newly defined *Hstx2* still operates as the X-linked hybrid sterility factor, controls meiotic chromosome synapsis, and modifies recombination rate. Optical mapping of the *Hstx2* genomic region excluded inversion as a cause of recombination suppression and revealed a striking copy number polymorphism of the microRNA *Mir465* cluster.

Acknowledgments

We are grateful to Vladana Fotopulosova for technical support; Inken Beck for generation of knockout mice (https://www.phenogenomics.cz/); and Lukas Cermak, Nikol Balogova, and Tomas Lidak for help with Western blotting. We thank Simon Myers for the B6.$Prdm9^{Hu}$ mice, Attila Toth for HORMAD2 antibody, Cornelia Burkhardt and Sven Künzel for sample preparation and Bionano optical mapping, and Emil Parvanov and Sarka Takacova for comments. This work was supported by LQ1604 project of the National Sustainability Program II from the Ministry of Education, Youth and Sports of the Czech Republic, and by

Czech Science Foundation grant GA CR No. 16-01969S to J.F., and the Charles University Grant Agency, GA UK No. 22218 to D.L., L.O.-H. and Y.F.C. were supported by the Max Planck Society.

Literature Cited

Anderson, L. K., A. Reeves, L. M. Webb, and T. Ashley, 1999 Distribution of crossing over on mouse synaptonemal complexes using immunofluorescent localization of MLH1 protein. Genetics 151: 1569–1579.

Baker, C. L., S. Kajita, M. Walker, R. L. Saxl, N. Raghupathy *et al.*, 2015 PRDM9 drives evolutionary erosion of hotspots in Mus musculus through haplotype-specific initiation of meiotic recombination. PLoS Genet. 11: e1004916. https://doi.org/10.1371/journal.pgen.1004916

Balcova, M., B. Faltusova, V. Gergelits, T. Bhattacharyya, O. Mihola *et al.*, 2016 Hybrid sterility locus on chromosome X controls meiotic recombination rate in mouse. PLoS Genet. 12: e1005906. https://doi.org/10.1371/journal.pgen.1005906

Ball, R. L., Y. Fujiwara, F. Sun, J. Hu, M. A. Hibbs *et al.*, 2016 Regulatory complexity revealed by integrated cytological and RNA-seq analyses of meiotic substages in mouse spermatocytes. BMC Genomics 17: 628. https://doi.org/10.1186/s12864-016-2865-1

Baudat, F., J. Buard, C. Grey, A. Fledel-Alon, C. Ober *et al.*, 2010 PRDM9 is a major determinant of meiotic recombination hotspots in humans and mice. Science 327: 836–840. https://doi.org/10.1126/science.1183439

Bhattacharyya, T., S. Gregorova, O. Mihola, M. Anger, J. Sebestova *et al.*, 2013 Mechanistic basis of infertility of mouse intersubspecific hybrids. Proc. Natl. Acad. Sci. USA 110: E468–E477. https://doi.org/10.1073/pnas.1219126110

Bhattacharyya, T., R. Reifova, S. Gregorova, P. Simecek, V. Gergelits *et al.*, 2014 X chromosome control of meiotic chromosome synapsis in mouse inter-subspecific hybrids. PLoS Genet. 10: e1004088. https://doi.org/10.1371/journal.pgen.1004088

Brick, K., S. Thibault-Sennett, F. Smagulova, K. G. Lam, Y. Pu *et al.*, 2018 Extensive sex differences at the initiation of genetic recombination. Nature 561: 338–342. https://doi.org/10.1038/s41586-018-0492-5

Campbell, P., J. M. Good, and M. W. Nachman, 2013 Meiotic sex chromosome inactivation is disrupted in sterile hybrid male house mice. Genetics 193: 819–828. https://doi.org/10.1534/genetics.112.148635

Chan, S., E. Lam, M. Saghbini, S. Bocklandt, A. Hastie *et al.*, 2018 Structural variation detection and analysis using Bionano optical mapping. Methods Mol. Biol. 1833: 193–203. https://doi.org/10.1007/978-1-4939-8666-8_16

Collaborative Cross Consortium, 2012 The genome architecture of the Collaborative Cross mouse genetic reference population. Genetics 190: 389–401. https://doi.org/10.1534/genetics.111.132639

Cong, L., F. A. Ran, D. Cox, S. Lin, R. Barretto *et al.*, 2013 Multiplex genome engineering using CRISPR/Cas systems. Science 339: 819–823. https://doi.org/10.1126/science.1231143

Coyne, J. A., and H. A. Orr, 2004 *Speciation*, Sinauer Associates, Sunderland, Massachusetts.

Davies, B., E. Hatton, N. Altemose, J. G. Hussin, F. Pratto *et al.*, 2016 Re-engineering the zinc fingers of PRDM9 reverses hybrid sterility in mice. Nature 530: 171–176. https://doi.org/10.1038/nature16931

Dion-Côté, A. M., and D. A. Barbash, 2017 Beyond speciation genes: an overview of genome stability in evolution and speciation. Curr. Opin. Genet. Dev. 47: 17–23. https://doi.org/10.1016/j.gde.2017.07.014

Dobzhansky, T., 1951 *Genetics and the origin of Species*, Columbia University, New York.

Duvaux, L., K. Belkhir, M. Boulesteix, and P. Boursot, 2011 Isolation and gene flow: inferring the speciation history of European house mice. Mol. Ecol. 20: 5248–5264. https://doi.org/10.1111/j.1365-294X.2011.05343.x

Dzur-Gejdosova, M., P. Simecek, S. Gregorova, T. Bhattacharyya, and J. Forejt, 2012 Dissecting the genetic architecture of f(1) hybrid sterility in house mice. Evolution 66: 3321–3335. https://doi.org/10.1111/j.1558-5646.2012.01684.x

Ernst, C., N. Eling, C. P. Martinez-Jimenez, J. C. Marioni, and D. T. Odom, 2019 Staged developmental mapping and X chromosome transcriptional dynamics during mouse spermatogenesis. Nat. Commun. 10: 1251. https://doi.org/10.1038/s41467-019-09182-1

Flachs, P., O. Mihola, P. Simecek, S. Gregorova, J. Schimenti *et al.*, 2012 Interallelic and intergenic incompatibilities of the Prdm9 (Hst1) gene in mouse hybrid sterility. PLoS Genet. 8: e1003044. https://doi.org/10.1371/journal.pgen.1003044

Flachs, P., T. Bhattacharyya, O. Mihola, J. Pialek, J. Forejt *et al.*, 2014 Prdm9 incompatibility controls oligospermia and delayed fertility but no selfish transmission in mouse intersubspecific hybrids. PLoS One 9: e95806. https://doi.org/10.1371/journal.pone.0095806

Flint, J., W. Valdar, S. Shifman, and R. Mott, 2005 Strategies for mapping and cloning quantitative trait genes in rodents. Nat. Rev. Genet. 6: 271–286. https://doi.org/10.1038/nrg1576

Forejt, J., 1996 Hybrid sterility in the mouse. Trends Genet. 12: 412–417. https://doi.org/10.1016/0168-9525(96)10040-8

Forejt, J., and P. Ivanyi, 1974 Genetic studies on male sterility of hybrids between laboratory and wild mice (Mus musculus L.). Genet. Res. 24: 189–206. https://doi.org/10.1017/S0016672300015214

Forejt, J., J. Pialek, and Z. Trachtulec, 2012 Hybrid male sterility genes in the mouse subspecific crosses, pp. 482–503 in *Evolution of the House Mouse*, edited by Macholan, M., S. J. E. Baird, P. Muclinger, and J. Pialek. Cambridge University Press, Cambridge. https://doi.org/10.1017/CBO9781139044547.021

Fuller, Z. L., C. J. Leonard, R. E. Young, S. W. Schaeffer, and N. Phadnis, 2018 Ancestral polymorphisms explain the role of chromosomal inversions in speciation. PLoS Genet. 14: e1007526. https://doi.org/10.1371/journal.pgen.1007526

Garcia-Muse, T., U. Galindo-Diaz, M. Garcia-Rubio, J. S. Martin, J. Polanowska *et al.*, 2019 A meiotic checkpoint Alters repair partner bias to permit inter-sister repair of persistent DSBs. Cell Rep. 26: 775–787.e5. https://doi.org/10.1016/j.celrep.2018.12.074

Good, J. M., M. D. Dean, and M. W. Nachman, 2008 A complex genetic basis to X-linked hybrid male sterility between two species of house mice. Genetics 179: 2213–2228. https://doi.org/10.1534/genetics.107.085340

Gregorova, S., and J. Forejt, 2000 PWD/Ph and PWK/Ph inbred mouse strains of Mus m. musculus subspecies–a valuable resource of phenotypic variations and genomic polymorphisms. Folia Biol. (Praha) 46: 31–41.

Gregorová, S., M. Mnuková-Fajdelová, Z. Trachtulec, J. Capková, M. Loudová *et al.*, 1996 Sub-milliMorgan map of the proximal part of mouse Chromosome 17 including the hybrid sterility 1 gene. Mamm. Genome 7: 107–113. https://doi.org/10.1007/s003359900029

Gregorova, S., V. Gergelits, I. Chvatalova, T. Bhattacharyya, B. Valiskova *et al.*, 2018 Modulation of Prdm9-controlled meiotic chromosome asynapsis overrides hybrid sterility in mice. eLife 7: e34282. https://doi.org/10.7554/eLife.34282

Haldane, J., 1922 Sex ration and unisexual sterility in hybrid animals. J. Genet. 12: 101–109. https://doi.org/10.1007/BF02983075

Hammer, M. F., F. L. Mendez, M. P. Cox, A. E. Woerner, and J. D. Wall, 2008 Sex-biased evolutionary forces shape genomic

patterns of human diversity. PLoS Genet. 4: e1000202. https://doi.org/10.1371/journal.pgen.1000202
Harr, B., E. Karakoc, R. Neme, M. Teschke, C. Pfeifle *et al.*, 2016 Genomic resources for wild populations of the house mouse, Mus musculus and its close relative Mus spretus. Sci. Data 3: 160075. https://doi.org/10.1038/sdata.2016.75
Hinch, A. G., G. Zhang, P. W. Becker, D. Moralli, R. Hinch *et al.*, 2019 Factors influencing meiotic recombination revealed by whole-genome sequencing of single sperm. Science 363: eaau8861. https://doi.org/10.1126/science.aau8861
Hooper, D. M., S. C. Griffith, and T. D. Price, 2018 Sex chromosome inversions enforce reproductive isolation across an avian hybrid zone. Mol. Ecol. 28: 1246–1262.
Janoušek, V., L. Wang, K. Luzynski, P. Dufkova, M. M. Vyskocilova *et al.*, 2012 Genome-wide architecture of reproductive isolation in a naturally occurring hybrid zone between Mus musculus musculus and M. m. domesticus. Mol. Ecol. 21: 3032–3047. https://doi.org/10.1111/j.1365-294X.2012.05583.x
Jung, M., D. Wells, J. Rusch, S. Ahmad, J. Marchini *et al.*, 2019 Unified single-cell analysis of testis gene regulation and pathology in five mouse strains. Elife. 25: 8. https://doi.org/10.7554/eLife.43966
Kirkpatrick, M., 2010 How and why chromosome inversions evolve. PLoS Biol. 8: e1000501. https://doi.org/10.1371/journal.pbio.1000501
Lange, J., S. Yamada, S. E. Tischfield, J. Pan, S. Kim *et al.*, 2016 The Landscape of Mouse Meiotic Double-Strand Break Formation, Processing, and Repair. Cell 167: 695–708.e16. https://doi.org/10.1016/j.cell.2016.09.035
Larson, E. L., S. Keeble, D. Vanderpool, M. D. Dean, and J. M. Good, 2016 The composite regulatory basis of the large X-effect in mouse speciation. Mol. Biol. Evol. 34: 282–295.
Mack, K. L., and M. W. Nachman, 2017 Gene regulation and speciation. Trends Genet. 33: 68–80. https://doi.org/10.1016/j.tig.2016.11.003
Macholán, M., S. J. Baird, P. Dufkova, P. Munclinger, B. V. Bimova *et al.*, 2011 Assessing multilocus introgression patterns: a case study on the mouse X chromosome in central Europe. Evolution 65: 1428–1446. https://doi.org/10.1111/j.1558-5646.2011.01228.x
Macholán, M., P. Munclinger, M. Sugerkova, P. Dufkova, B. Bimova *et al.*, 2007 Genetic analysis of autosomal and X-linked markers across a mouse hybrid zone. Evolution 61: 746–771. https://doi.org/10.1111/j.1558-5646.2007.00065.x
Maheshwari, S., and D. A. Barbash, 2011 The genetics of hybrid incompatibilities. Annu. Rev. Genet. 45: 331–355. https://doi.org/10.1146/annurev-genet-110410-132514
Margolin, G., P. P. Khil, J. Kim, M. A. Bellani, and R. D. Camerini-Otero, 2014 Integrated transcriptome analysis of mouse spermatogenesis. BMC Genomics 15: 39. https://doi.org/10.1186/1471-2164-15-39
Mihola, O., Z. Trachtulec, C. Vlcek, J. C. Schimenti, and J. Forejt, 2009 A mouse speciation gene encodes a meiotic histone H3 methyltransferase. Science 323: 373–375. https://doi.org/10.1126/science.1163601
Miyata, H., J. M. Castaneda, Y. Fujihara, Z. Yu, D. R. Archambeault *et al.*, 2016 Genome engineering uncovers 54 evolutionarily conserved and testis-enriched genes that are not required for male fertility in mice. Proc. Natl. Acad. Sci. USA 113: 7704–7710. https://doi.org/10.1073/pnas.1608458113
Morgan, A. P., D. M. Gatti, M. L. Najarian, T. M. Keane, R. J. Galante *et al.*, 2017 Structural variation shapes the landscape of recombination in mouse. Genetics 206: 603–619. https://doi.org/10.1534/genetics.116.197988
Myers, S., R. Bowden, A. Tumian, R. E. Bontrop, C. Freeman *et al.*, 2010 Drive against hotspot motifs in primates implicates the PRDM9 gene in meiotic recombination. Science 327: 876–879. https://doi.org/10.1126/science.1182363
Nachman, M. W., and B. A. Payseur, 2012 Recombination rate variation and speciation: theoretical predictions and empirical results from rabbits and mice. Philos. Trans. R. Soc. Lond. B Biol. Sci. 367: 409–421. https://doi.org/10.1098/rstb.2011.0249
Orr, H. A., 2005 The genetic basis of reproductive isolation: insights from Drosophila. Proc. Natl. Acad. Sci. USA 102: 6522–6526. https://doi.org/10.1073/pnas.0501893102
Ortiz-Barrientos, D., J. Engelstadter, and L. H. Rieseberg, 2016 Recombination rate evolution and the origin of species. Trends Ecol. Evol. 31: 226–236. https://doi.org/10.1016/j.tree.2015.12.016
Ota, H., Y. Ito-Matsuoka, and Y. Matsui, 2019 Identification of the X-linked germ cell specific miRNAs (XmiRs) and their functions. PLoS One 14: e0211739. https://doi.org/10.1371/journal.pone.0211739
Parvanov, E. D., P. M. Petkov, and K. Paigen, 2010 Prdm9 controls activation of mammalian recombination hotspots. Science 327: 835. https://doi.org/10.1126/science.1181495
Patten, M. M., 2018 Selfish X chromosomes and speciation. Mol. Ecol. 27: 3772–3782. https://doi.org/10.1111/mec.14471
Payseur, B. A., J. G. Krenz, and M. W. Nachman, 2004 Differential patterns of introgression across the X chromosome in a hybrid zone between two species of house mice. Evolution 58: 2064–2078. https://doi.org/10.1111/j.0014-3820.2004.tb00490.x
Payseur, B. A., D. C. Presgraves, and D. A. Filatov, 2018 Introduction: sex chromosomes and speciation. Mol. Ecol. 27: 3745–3748. https://doi.org/10.1111/mec.14828
Phifer-Rixey, M., and M. W. Nachman, 2015 Insights into mammalian biology from the wild house mouse Mus musculus. eLife 4: e05959. https://doi.org/10.7554/eLife.05959
Presgraves, D. C., 2018 Evaluating genomic signatures of "the large X-effect" during complex speciation. Mol. Ecol. 27: 3822–3830. https://doi.org/10.1111/mec.14777
Royo, H., G. Polikiewicz, S. K. Mahadevaiah, H. Prosser, M. Mitchell *et al.*, 2010 Evidence that meiotic sex chromosome inactivation is essential for male fertility. Curr. Biol. 20: 2117–2123. https://doi.org/10.1016/j.cub.2010.11.010
Royo, H., H. Seitz, E. ElInati, A. H. Peters, M. B. Stadler *et al.*, 2015 Silencing of X–linked MicroRNAs by meiotic sex chromosome inactivation. PLoS Genet. 11: e1005461. https://doi.org/10.1371/journal.pgen.1005461
Sharan, S. K., L. C. Thomason, S. G. Kuznetsov, and D. L. Court, 2009 Recombineering: a homologous recombination-based method of genetic engineering. Nat. Protoc. 4: 206–223. https://doi.org/10.1038/nprot.2008.227
Smagulova, F., K. Brick, Y. M. Pu, R. D. Camerini-Otero, and G. V. Petukhova, 2016 The evolutionary turnover of recombination hot spots contributes to speciation in mice. Genes Dev. 30: 266–280. https://doi.org/10.1101/gad.270009.115
Spies, M., and R. Fishel, 2015 Mismatch repair during homologous and homeologous recombination. Cold Spring Harb. Perspect. Biol. 7: a022657. https://doi.org/10.1101/cshperspect.a022657
Srivastava, A., A. P. Morgan, M. L. Najarian, V. K. Sarsani, J. S. Sigmon *et al.*, 2017 Genomes of the mouse collaborative cross. Genetics 206: 537–556. https://doi.org/10.1534/genetics.116.198838
Storchová, R., S. Gregorova, D. Buckiova, V. Kyselova, P. Divina *et al.*, 2004 Genetic analysis of X-linked hybrid sterility in the house mouse. Mamm. Genome 15: 515–524. https://doi.org/10.1007/s00335-004-2386-0
Trachtulec, Z., M. Mnukova-Fajdelova, R. M. Hamvas, S. Gregorova, W. E. Mayer *et al.*, 1997 Isolation of candidate hybrid sterility 1 genes by cDNA selection in a 1.1 megabase pair region on mouse chromosome 17. Mamm. Genome 8: 312–316. https://doi.org/10.1007/s003359900430
Truett, G. E., P. Heeger, R. L. Mynatt, A. A. Truett, J. A. Walker *et al.*, 2000 Preparation of PCR-quality mouse genomic DNA

with hot sodium hydroxide and tris (HotSHOT). Biotechniques 29: 52, 54. https://doi.org/10.2144/00291bm09

Tucker, P., R. Sage, J. Warner, A. Wilson, and E. Eicher, 1992 Abrupt cline for sex chromosomes in a hybrid zone between two species of mice. Evolution 46: 1146–1163. https://doi.org/10.1111/j.1558-5646.1992.tb00625.x

Turner, L. M., D. J. Schwahn, and B. Harr, 2012 Reduced male fertility is common but highly variable in form and severity in a natural house mouse hybrid zone. Evolution 66: 443–458. https://doi.org/10.1111/j.1558-5646.2011.01445.x

Wang, L., B. Valiskova, and J. Forejt, 2018 Cisplatin-induced DNA double-strand breaks promote meiotic chromosome synapsis in PRDM9-controlled mouse hybrid sterility. eLife 7: e42511. https://doi.org/10.7554/eLife.42511

Wojtasz, L., J. M. Cloutier, M. Baumann, K. Daniel, J. Varga *et al.*, 2012 Meiotic DNA double-strand breaks and chromosome asynapsis in mice are monitored by distinct HORMAD2-independent and -dependent mechanisms. Genes Dev. 26: 958–973. https://doi.org/10.1101/gad.187559.112

Wu, G., W. Wang, Y. Liu, K. Zhuang, T. Cai *et al.*, 2018 RETRACTED: NY-SAR-35 is involved in apoptosis, cell migration, invasion and epithelial to mesenchymal transition in glioma. Biomed. Pharmacother. 97: 1632–1638. https://doi.org/10.1016/j.biopha.2017.11.076

Zhang, F., Y. Zhang, X. Lv, B. Xu, H. Zhang *et al.*, 2019 Evolution of an X–linked miRNA family predominantly expressed in mammalian male germ cells. Mol. Biol. Evol. 36: 663–678. https://doi.org/10.1093/molbev/msz001

Zhang, L., T. Sun, F. Woldesellassie, H. Xiao, and Y. Tao, 2015 Sex ratio meiotic drive as a plausible evolutionary mechanism for hybrid male sterility. PLoS Genet. 11: e1005073. https://doi.org/10.1371/journal.pgen.1005073

Communicating editor: F. Cole